

Title

Correlation between oxygen evolution reaction activity and surface compositional evolution in epitaxial $\text{La}_{0.5}\text{Sr}_{0.5}\text{Ni}_{1-x}\text{Fe}_x\text{O}_{3-\delta}$ thin films

Author Names and affiliations

Prajwal Adiga¹, Le Wang^{2,*}, Cindy Wong¹, Bethany E. Matthews³, Mark E. Bowden⁴, Steven R. Spurgeon^{3,5}, George E. Sterbinsky⁶, Monika Blum,^{7,8} Min-Ju Choi², Jinhui Tao², Tiffany C. Kaspar², Scott A. Chambers², Kelsey A. Stoerzinger^{1,2,*}, Yingge Du²

¹ School of Chemical, Biological and Environmental Engineering, Oregon State University, Corvallis, Oregon, 97331, USA

² Physical and Computational Sciences Directorate, Pacific Northwest National Laboratory, Richland, Washington 99354, USA

³ Energy and Environment Directorate, Pacific Northwest National Laboratory, Richland, Washington 99352, USA

⁴ Environmental Molecular Sciences Laboratory, Pacific Northwest National Laboratory, Richland, Washington 99352, USA

⁵ Department of Physics, University of Washington, Seattle, Washington 98195, USA

⁶ Advanced Photon Source, Argonne National Laboratory, Lemont, Illinois 60439, USA

⁷ Advanced Light Source, Lawrence Berkeley National Laboratory, Berkeley, California 94720 USA

⁸ Chemical Sciences Division, Lawrence Berkeley National Laboratory, Berkeley, California 94720 USA

Corresponding author

* Email address: le.wang@pnnl.gov; kelsey.stoerzinger@oregonstate.edu

Abstract

Water electrolysis can use renewable electricity to produce green hydrogen, a portable fuel and sustainable chemical precursor. Improving electrolyzer efficiency hinges on the activity of the oxygen evolution reaction (OER) catalyst. Earth-abundant, ABO_3 -type perovskite oxides offer great compositional, structural, and electronic tunability, with previous studies showing compositional substitution can increase the OER activity drastically. However, the relationship between the tailored bulk composition and that of the surface, where OER occurs, remains unclear. Here, we study the effects of electrochemical cycling on the OER activity of $\text{La}_{0.5}\text{Sr}_{0.5}\text{Ni}_{1-x}\text{Fe}_x\text{O}_{3-\delta}$ ($x = 0-0.5$) epitaxial films grown by oxide molecular beam epitaxy as a model Sr-containing perovskite oxide. Electrochemical testing and surface-sensitive spectroscopic analyses show Ni segregation, which is affected by electrochemical history, along with surface amorphization, coupled with changes in OER activity. Our findings highlight the importance of surface composition and electrochemical cycling conditions in understanding OER performance, suggesting common motifs of the active surface with high surface area systems.

Keywords

surface reconstruction, Ni segregation, perovskite oxides, heteroatom doping

Introduction

Water electrolysis is central to the development of sustainable energy storage and a pathway towards a hydrogen-based economy.¹ Electrolyzer efficiency is limited by the high overpotentials required for the anodic oxygen evolution reaction (OER).² ABO₃-type perovskite oxides have gained traction as promising OER catalysts in alkaline electrolytes owing to their low cost, environmental friendliness, and structural and electronic tunability.³⁻⁹

Perovskite LaNiO₃ (LNO) has been extensively studied as Ni³⁺ offers moderate binding of reaction intermediates and high Ni-O covalency, leading to high OER activity. The incorporation of heteroatoms into the LNO structure has been regarded as one of the most facile and effective strategies to optimize catalytic performance.¹⁰⁻¹⁵ For example, A-site substitution of La³⁺ with Sr²⁺ in LNO improves OER activity by inducing an upward shift of the O 2p bands relative to the Fermi level, strengthening Ni 3d-O 2p hybridization, and decreasing charge transfer energy.¹² On the other hand, B-site doping with non-noble transition metals (e.g. Fe, Co) can strongly tune the 3d-orbital states near the Fermi level, showing a notable influence on OER activity as well.^{14, 15} In addition, dual-site doping in La_{1-x}Sr_xNi_{1-x}Fe_xO₃ has been found by Fu *et al.* to yield holes mainly characteristic of Fe (vs Ni), with claims that the Fe⁴⁺ state is crucial for enhancing OER activity by six times compared to pure LNO.¹⁶ While these studies focus on transition metal cation active sites, recent studies have shown that the lattice oxygen of LNO participates in the formation of reaction intermediates as well, enabling higher OER activity via the lattice oxygen mechanism (LOM).^{17, 18}

It has been reported that the surface of some perovskites, especially those containing Sr,¹⁹ can lose their crystalline structure after OER. This can yield a local coordination environment resembling oxyhydroxides that are known to form on simple Ni and Fe oxides. In these oxyhydroxides, changes in Ni redox features induced by Fe-incorporation, coupled with changes OER activity, are known to occur with cycling.²⁰⁻²² For Sr-containing perovskites, it is likely that some degree of Sr-leaching in an alkaline electrolyte might also lead to a transition-metal rich surface phase under OER conditions; the properties and resultant performance of the surface might change with cycling like in Ni-Fe oxyhydroxide materials.²³⁻²⁵

Herein, we report the cycling- and potential-scan-window- dependent OER activity of La_{0.5}Sr_{0.5}Ni_{1-x}Fe_xO_{3-δ} (LSNFO with x = 0, 0.125, 0.25, 0.375, and 0.5) solid solution epitaxial films. The surface Ni redox behavior is used to understand the change of surface composition along with atomic force microscopy (AFM), X-ray photoelectron

spectroscopy (XPS) and transmission electron microscopy (TEM) on pristine and post-cycled films. We find that activity generally increases with cycling, as does the integrated charge of the Ni redox feature. OER activity is maximum for $x = 0.25$, which is lower in Fe content compared to that with the highest OER activity for $\text{LaNi}_{1-x}\text{Fe}_x\text{O}_{3-\delta}$ ($x = 0.375$)¹⁴, and the surface forms an amorphous layer depleted in Sr after cycling. These results emphasize that “intrinsic” OER activity for Ni- and Fe-containing perovskite oxides must consider possible changes at the surface in order to clearly understand the descriptors of catalytic activity.

Results and discussion

Structural and electronic characterization

LSNFO epitaxial thin films of 20 unit cells thickness were grown on (001)-oriented $(\text{LaAlO}_3)_{0.3}(\text{Sr}_2\text{AlTaO}_6)_{0.7}$ (LSAT) substrates using oxygen-plasma-assisted molecular beam epitaxy (OPA-MBE).¹⁴ The X-ray diffraction (XRD) θ - 2θ scans near the (002) peak for various Fe compositions (x) shown in Fig. 1a exhibit well-defined Kiessig fringes, confirming their high structural quality. Extended XRD θ - 2θ scans of LSNFO samples are shown in Fig. S1a. Representative reciprocal space maps (RSMs, Fig. S1c) reveal that these films are coherently strained. Fig. S1c shows the out-of-plane lattice parameter (c) for LSNFO as a function of x . Compared with the pseudo-cubic lattice constants for bulk LNO and SrNiO_3 ,^{26, 27} the larger value of c for $x = 0$ suggests that these solid solution samples may contain non-negligible amounts of oxygen vacancies.²⁸ In-plane transport measurements (Fig. S1d) shows metallic behavior for $x \leq 0.375$, but semiconducting behavior for $x = 0.5$. X-ray photoelectron spectroscopy (XPS) analysis (Fig. 1b) on pristine samples indicate that the surface composition is comparable to that expected from target stoichiometry. To determine the B-site cation valences in LSNFO, Ni K -edge and Fe K -edge X-ray absorption near-edge structure (XANES) spectra were measured (shown in Fig. 1c, d). According to previous studies on Co-based materials,²⁹⁻³¹ the energy corresponding to normalized absorption of ≈ 0.8 can be used to determine the transition metal valence state. As shown in the inset of Fig. 1c, the energy position of Ni-K XANES spectra for the $x = 0$ sample locates between Ni^{2+} (NiO) and Ni^{3+} (LaNiO_3) references,¹⁴ demonstrating the existence of mixed $\text{Ni}^{2+/3+}$. With increasing x from 0 to 0.5, the Ni-K XANES spectra gradually shift to higher energy and approach that of Ni^{3+} reference, indicating the increase of Ni valence state with x . This is in contrast to LNFO (without Sr), in which average Ni valence state decreased with increasing Fe content.¹⁴ In contrast, films of all Fe content show nominally greater Fe oxidation state than a LaFeO_3 (Fe^{3+}) reference (see inset of Fig. 1d), indicating that Sr-substitution in the mixed Ni-Fe perovskite oxides primarily increases the nominal Fe oxidation state.

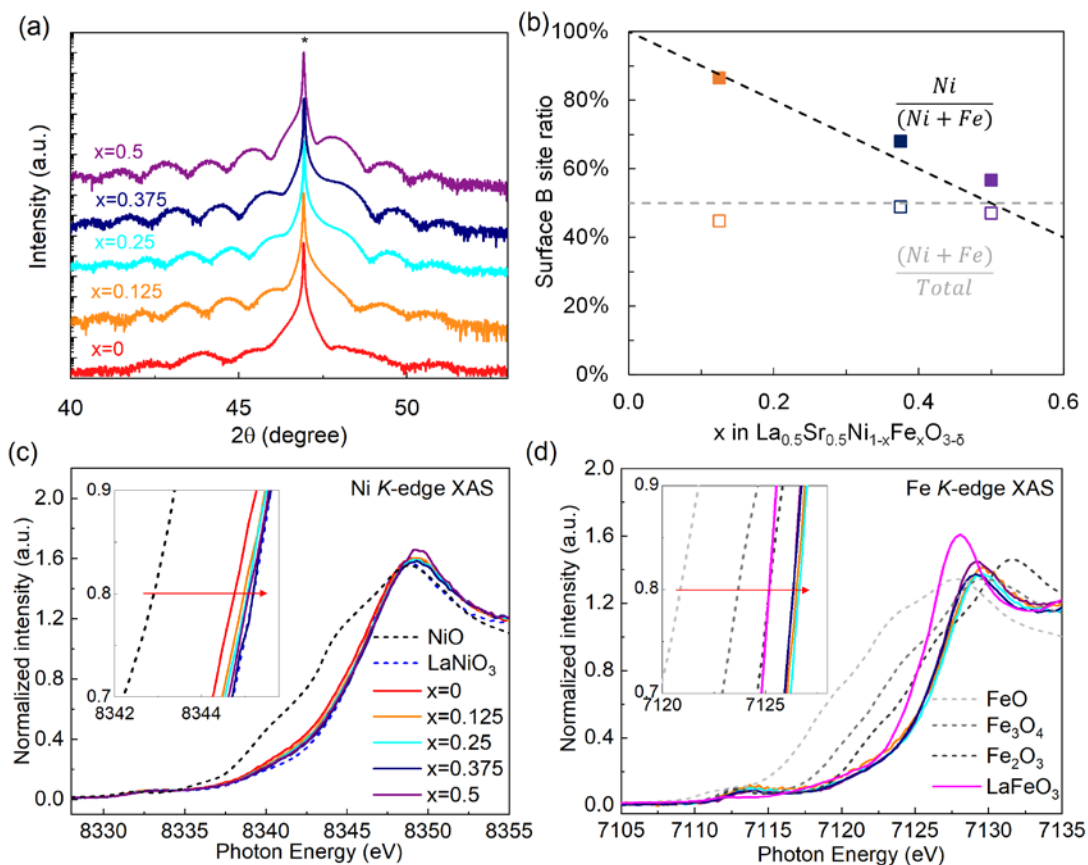


Fig. 1 Structural characterization and XANES spectra at the *K*-edge for LSNFO epitaxial thin films. (a) High-resolution XRD θ - 2θ scans show high film quality. (b) XPS composition ratios of Ni to total B (Fe+Ni) sites (solid markers) and total B sites to total metal (La+Sr+Fe+Ni) sites (hollow markers) show the decrease in surface Ni sites as expected (dashed black trendline) with increasing x and comparable B sites to total elemental sites (dashed grey trendline) across x . (c) Ni *K*-edge XAS. (d) Fe *K*-edge XAS.

OER activity assessment

We next investigate the impact of dual-site doping of LSNFO electrocatalysts on the OER activities in 0.1 M KOH solution by cyclic voltammetry (CV, Fig. 2 and Fig. S2). Similar to LSNO with 50% Sr content¹², the OER activity of LSNFO increases with cycling. To better understand the link between electrochemical potential and time in driving these changes, we compare the OER activity measured by CVs across the potential profile shown schematically in Fig. 2a. Fig. 2b shows the Ni redox features for $x = 0.375$ under CV-1, CV-2 and CV-3 cycling conditions, where Ni redox generally shifts to higher potentials or remains similar but increasing in total charge. For CV-3, comparing electrodes with different Fe compositions (Fig. 2c), we see distinct

differences in the Ni redox features, especially for $x = 0.375$ and $x = 0.5$ where a second Ni reduction feature at ~ 1.37 V vs RHE is observed.

Upon initial cycling (CV-1), OER activity is maximum for $x = 0.125$, quantified by either the highest current density (j) at 1.6 V vs RHE (Fig. 2d) or the lowest overpotential (η) to achieve a current density of $100 \mu\text{A}/\text{cm}^2$ (Fig. 2e). The current density at 1.6 V vs RHE for $x = 0.125$ is five times higher than that of $\text{LaNi}_{1-x}\text{Fe}_x\text{O}_3$ (LNFO) without Sr. We also find that incorporating Sr in LNFO shifts the maximum in OER activity to lower x (maximum at $x = 0.375$ for LNFO).¹⁴ Ni redox features shift to higher anodic potential with increasing x , consistent with the LNFO system and previous reports of Ni-Fe oxide catalysts.^{14, 32, 33} In such systems, this shift arises from charge transfer from Fe to Ni, making Ni more difficult to oxidize with increasing Fe content. In addition, the separation between Ni reduction and oxidation is comparable for all films during CV-1 (Fig. 2f), about 82 mV, similar to literature for other Ni-Fe oxides and somewhat larger than the 60 mV typically reported for reversible processes.^{34, 35}

Following an initial set of CVs (CV-1) and chronoamperometry (CA), we then repeat a series of CVs over the same potential range (CV-2) to quantify activity and Ni redox. For CV-2, OER activity increases significantly for $x = 0.25$ while slightly for $x = 0.375$ and $x = 0.5$, using either j or η as metrics. Similar trends in OER activity are observed for the preceding CA, with Tafel slopes ranging from ~ 78 mV/decade ($x = 0$) to 49 mV/decade ($x = 0.25$) (Fig. S3). For $x = 0.25$, this is commensurate with the appearance on Ni redox at surprisingly high applied potentials given the small amount of Fe incorporation but at peak spacing comparable to that of $x = 0$ (and greater than that of CV-1). We note, however, that similarly high Ni redox features have been observed for $\text{Ni}_{0.75}\text{Fe}_{0.25}(\text{OH})_2$ films.³³

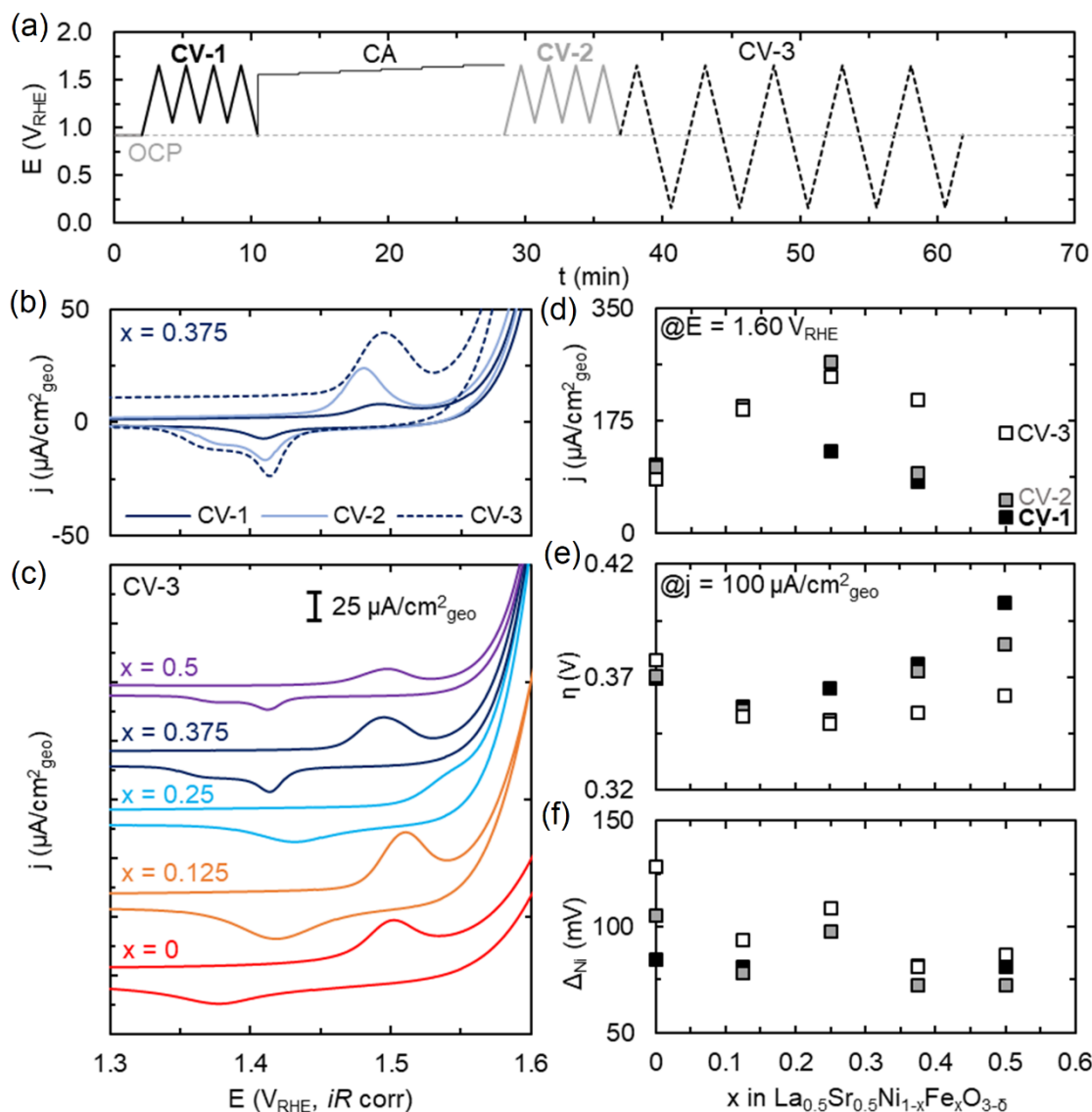


Fig. 2 Electrochemical measurements of LSNFO epitaxial films. (a) Experimental protocol showing working electrode potential on the RHE scale as a function of time (t). (b) Cyclic voltammetry (CV) at 10 mV/s as a function of electrochemical cycling window (CV-1, 2, 3) for $x = 0.375$ shows differences in Ni redox position and an evolving secondary Ni reduction peak. (c) CV-3 for the 2nd cycle across Fe compositions from 0 to 0.5 shows changing Ni redox feature and position. (d) Ni redox peak separation (Δ_{Ni}), (e) OER overpotential (η) and (f) current density at 1.60 V_{RHE} for the 2nd cycle of the three CV scans (color coding as per Fig. 2(a)) as a function of Fe content (x) in LSNFO.

To better understand the role of Fe on the surface in OER, we then cycle to potentials low enough to undergo Fe redox (CV-3). As expected, the integrated charge associated with Fe reduction increases with x (Fig. S4). Cycling to such low potentials results in

large increases in activity for films with high Fe content ($x = 0.375, 0.5$). This is generally accompanied by an increase in Ni redox peak separation, suggesting changes in surface composition/structure and resultant properties. Furthermore, for films of $x = 0.375$ and greater, the Ni-reduction transforms from one to two distinct features starting in CV-2. This further suggests surface changes resultant from cycling, and surface changes are likely linked to the observed increase in OER activity. Similar split-reduction peaks have been observed in Fe–NiO_xH_y catalysts³⁴ and attributed to inhomogeneous distribution of Fe, particularly around the ~25% solubility limit of Fe in NiOOH.³⁶

Assessing changes to the electrode surface

Electrochemical cycling may impact i) available surface area (film roughness), ii) surface composition, and/or iii) surface structure, all of which would be expected to impact OER activity. To assess possible changes in surface roughness, we estimated the double layer capacitance (normalized to the electrode geometric area)³⁷ across the three CV windows (Fig. 3a). We observed a marginal increase in the double layer capacitance between CV-1 and CV-2. Upon sweeping the potentials into the Fe redox potentials (CV-3), a significant increase by ~ two times in the double layer capacitance is observed across all Fe compositions.

To assess whether this increase in capacitance is also commensurate with exposure of more OER active sites, we next consider the integrated charge of Ni redox (Fig. 3b), converted to an exposed number of Ni atoms/nm², n , using the perovskite unit cell and assuming redox corresponds to 1 e⁻ transfer.³³ We note others have classified this redox process as involving up to 1.6 e⁻,³⁸ which would result in our numbers overestimating the atomic density of Ni atoms on the surface. In CV-1, Ni surface content trends as expected with Fe incorporation, but is ~1/2 that expected from the unit cell size (assuming complete BO₂ termination of the (001) orientation) and target stoichiometry. This thus may originate from some persistence of AO termination at the surface. In CV-2, surface Ni content increases to approximately that expected based on stoichiometry for complete BO₂-layer termination, consistent with AO terminations dissolving during OER in highly alkaline media. Despite this ~2 fold increase in Ni redox current between CV-1 and CV-2, there is substantial change in OER current only for $x = 0.25$, suggesting the local arrangement of active sites, or number of exposed Fe sites, is most critical in driving activity. Upon sweeping into the Fe redox region (CV-3), surface Ni content further increases (Fig. 3b). For films with low Fe contents, the surface Ni content increases beyond that expected for a smooth film (assuming 1 e⁻/Ni during redox), indicating an increase in surface roughness or electrolyte permeability, commensurate with AFM and the large increase in capacitance. As a function of cycle number in CV-3 (inset in Fig. 3b), Ni redox increases while Fe redox decreases (Fig. S4), suggesting an evolution of surface composition during CV-3 cycling as well. A

slight enhancement in OER activity is also observed as a function of cycle number in CV-3.

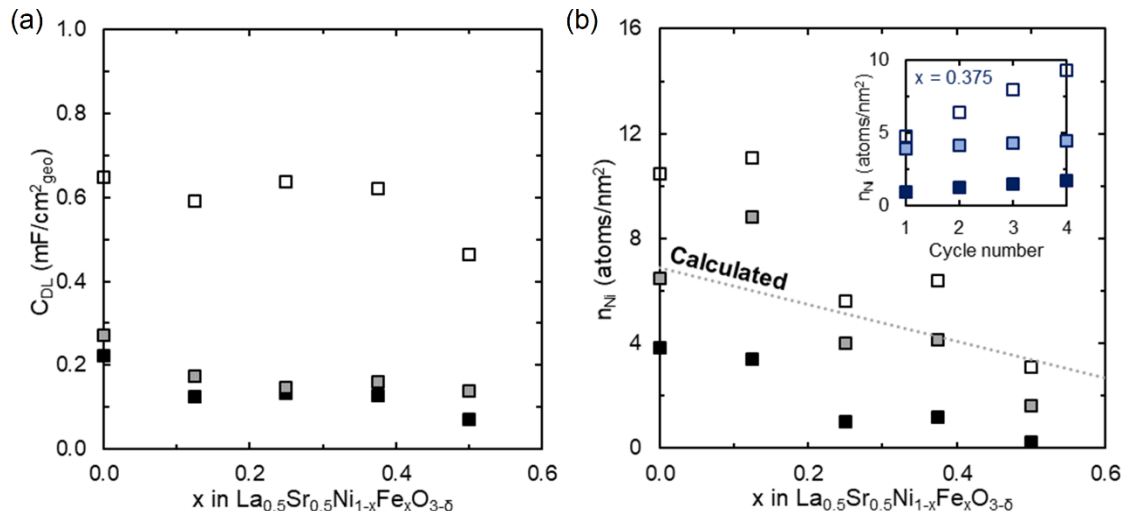


Fig. 3 Changes in LSNFO double layer capacitance and surface Ni composition with cycling. (a) Double layer capacitance (C_{DL}) normalized by the geometric area as a function of x in $\text{La}_{0.5}\text{Sr}_{0.5}\text{Ni}_{1-x}\text{Fe}_x\text{O}_{3-\delta}$. (b) Surface Ni atoms (n_{Ni}) per geometric nm^2 (obtained from Ni redox charge, see SI) as a function of x in $\text{La}_{0.5}\text{Sr}_{0.5}\text{Ni}_{1-x}\text{Fe}_x\text{O}_{3-\delta}$. The inset shows surface Ni atoms per geometric nm^2 for $x = 0.375$ as a function of cycle number, where shade decreases from CV-1 to CV-3.

In order to directly assess changes in surface structure and composition, we characterized the $x = 0.375$ sample before (pristine) and after electrochemical cycling. XRD θ -2 θ scans (Fig. 4a) show the diffraction peak of the LSNFO film shifts from the right side to the left side of the substrate's diffraction peak after cycling, indicating a larger lattice parameter. The disappearance of the thickness fringes suggests that the lattice structure becomes non-uniform after cycling. Atomic force microscopy (AFM) scans (Fig. S5) indicate that surface morphology changes from relatively flat to uneven and the arithmetic mean roughness (R_a) increases from 0.2 to ~ 1.1 nm after cycling. Cross-sectional scanning transmission electron microscopy (STEM) images (Fig. 4b) reveal that the surface is smooth for the pristine sample, while top 2 u.c. layer of the $x = 0.375$ sample becomes structurally amorphous after cycling. Energy dispersive X-ray spectroscopy (EDS) maps show that the pristine sample is mostly uniform in composition, but some regions of Ni segregation are also observed. After OER testing, more regions of Ni segregation are apparent, which may be related to the multiple Ni reduction peaks evident in later OER cycling. Fig. 4c shows the comparison of O 1s, Sr 3d, La 4d and Ni 3p & Fe 3p XPS core level spectra before and after cycling. To

compare the spectra quantitatively, we multiply all core level spectral intensities of the sample after cycling by 2.15 times to achieve a good overlap of Fe 2p spectra with that of the pristine sample. After cycling, the Ni 3p region is relatively more intense compared to the Fe 3p, suggesting that the Ni content on the surface increases after OER in agreement with electrochemical measurements. In addition, a distinct high binding energy shoulder is also observed on the Ni 3p spectrum after cycling, and shift of spectral weight to higher binding energies. Such changes in XPS could be due to Ni segregation at the surface region (Fig. 4b), and others have calculated a Ni oxyhydroxide-like surface on LNO after cycling, observing similar Ni 3p lineshapes.²⁵ Moreover, the decrease in Sr/La area ratio by XPS after cycling indicates Sr-leaching occurs during OER, which is common in Sr-based perovskite oxides,²³ and the width change of the La 4d spectrum after cycling suggests appreciable hydroxide character at the surface.³⁹ The O 1s shows a greater presence of adsorbed surface species after cycling, such as hydroxide, carbonate, and water.⁴⁰⁻⁴²

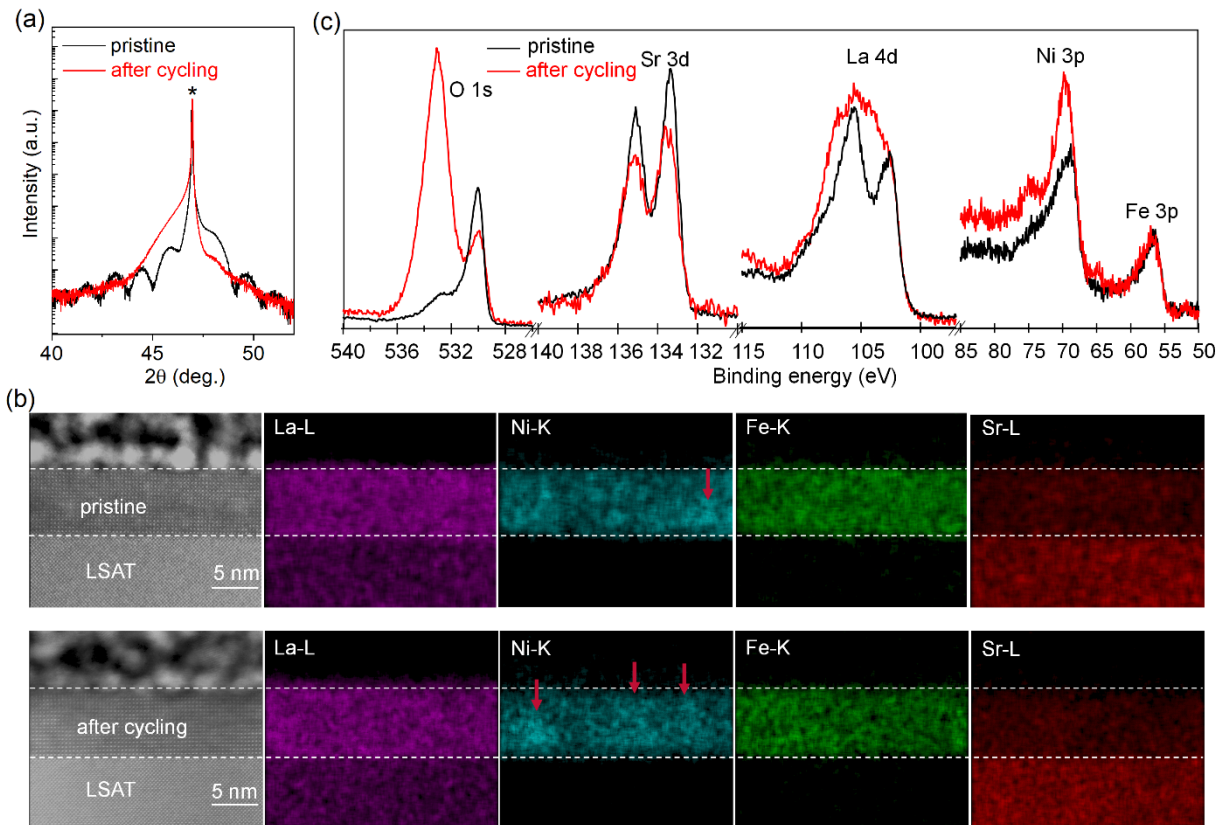


Fig. 4 XRD, STEM, EDS mapping, and XPS. (a) XRD θ -2 θ scans around the (002) diffraction peak, (b) Cross-sectional STEM images and EDS maps, and (c) comparison of O 1s, Sr 3d, La 4d, and Ni 3p & Fe 3p XPS core level spectra for the LSNFO ($x =$

0.375) film before (pristine) and after cycling. For comparison, all core level spectra intensity of the sample after cycling are multiplied by 2.15 times. The LSAT substrate peaks are marked with “*” in (a). White dashed lines and red arrows in (b) denote the interfaces of the pristine samples and the Ni segregation regions, respectively.

Implications on design of OER catalysts

Sr²⁺ substitution for La³⁺ in La-based perovskite oxides has broadly been reported to enhance transition metal 3d – O 2p covalency^{12, 42, 43}, boosting OER activity¹⁴. With substitution in a mixed Ni-Fe perovskite film, we observe that only Fe is oxidized (Fig. 1c, d), although the shift in Ni redox with Fe incorporation suggests that Ni at the surface indeed becomes harder to oxidize with Fe incorporation, similar to the case of LNFO¹⁴ and other Ni-Fe oxides^{32, 33}. Compared to LNFO,¹⁴ Sr-substitution in LNFO shifts the maximum OER activity to lower Fe contents (x=0.25 vs x=0.375 for LNFO) but with similar maximum current density (~0.21 mA/cm² at 1.6 V vs RHE) for each optimum composition.

Considering changes in Ni redox with cycling, the incorporation of Sr appears to promote surface restructuring with cycling, evident by the decrease in Sr/La ratio by XPS and depletion of Sr at the surface in STEM EDS after cycling. Roughness in AFM after cycling is consistent with such restructuring, commensurate with the appearance of split Ni reduction features for x=0.375 and greater, suggesting local composition variation for Fe contents exceeding the solubility limit in a possible NiOOH surface phase. Similar split-reduction peaks have been observed in Fe–NiO_xH_y catalysts³⁴ and attributed to inhomogeneous distribution of Fe, particularly around the ~25% solubility limit of Fe in NiOOH.³⁶ Here we observe a ~2 u.c. amorphous layer for an LSNFO film after 15 cycles in addition to chronoamperometry. This suggests that the surface of LSNFO films may in time draw many parallels to the Ni-Fe hydroxide films broadly studied for OER as well, which similarly show maximum activity for ~25% Fe.³⁶ Our findings also indicate that covalency of Fe-O sites are critical to enhancing OER activity—as bulk trends in Ni oxidation state or surface assessment of available Ni sites are not reflected in activity. The local environment of these active Fe sites may change notably during measurement, in particular when bulk Fe is present in the material and may redistribute/deposit with cycling. This study illustrates that although the underlying bulk materials template does impact OER activity, designing and controlling the active phase requires detailed understanding of surface restructuring during OER conditions, here borne out through systematic study of epitaxial thin films.

Conclusion

In this study, we report the electrocatalytic OER activity of La_{0.5}Sr_{0.5}Ni_{1-x}Fe_xO_{3-δ} epitaxial thin films (x = 0-0.5) and show activity depends not only on bulk Fe content but also on

the extent and window of electrochemical cycling. In comparison to previous work on $\text{LaNi}_{1-x}\text{Fe}_x\text{O}_3$, where Fe was oxidized at the expense of Ni reduction, Sr-incorporation results in Fe oxidation and generally maintains nominal Ni^{3+} character. Despite these trends in bulk chemistry, electrochemical potentials of Ni oxidation are still influenced by the local presence of Fe, suggesting a dynamic interplay at the surface under OER conditions. Sr incorporation promotes surface restructuring (confirmed using STEM), leading to an amorphous surface layer depleted of Sr. Electrochemical cycling suggests rearrangement at the surface via increasing Ni redox charge, however this is not directly mirrored in OER activity. Instead, excursion to Fe reduction potentials leads to the largest increase in activity for select compositions, suggesting Fe-O covalency is more likely the origin of increased activity for $x=0.25$. These findings suggest that although bulk composition can provide a template for understanding activity trends, the intrinsic activity of covalent perovskites with alkaline-earth A-sites is highly dependent on electrochemical cycling conditions due to the dynamic nature of surface composition.

Author contributions

P.A. Investigation, Writing – original draft, Writing – review & editing, L.W. Investigation, Writing – original draft, Writing – review & editing, Conceptualization, C.W. Investigation, B.E.M. Investigation, M.E.B. Investigation, S.R.S. Investigation, G.E.S. Investigation, M.B. Investigation, M.-J.C. Investigation, J.T. Supervision, T.C.K. Investigation, S.A.C. Supervision, Funding acquisition, K.A.S. Supervision, Writing – review & editing, Conceptualization, Funding acquisition, Y.D. Supervision, Writing – review & editing, Funding acquisition.

Conflicts of interests

There are no conflicts to declare

Acknowledgements

Synthesis of epitaxial thin films, X-ray diffraction, XPS, XAS, AFM, and STEM were supported by U.S. DOE BES Materials Science and Engineering Division under Award No. 10122. OER studies, additional AFM, and AP-XPS were supported by the National Science Foundation under Grant No. 2041153. P.A. acknowledges support from the Link Foundation Energy Fellowship. K.A.S. acknowledges support from Oregon State University as a Callahan Faculty Scholar. Part of this research (AFM) was conducted at Oregon Process Innovation Center, part of the Northwest Nanotechnology Infrastructure, a National Nanotechnology Coordinated Infrastructure site at Oregon State University which is supported in part by the National Science Foundation (grant NNCI-2025489) and Oregon State University. This research used resources of the

Advanced Light Source, a U.S. DOE Office of Science User Facility under contract no. DE-AC02-05CH11231. We acknowledge facility support from W. R. Wiley Environmental Molecular Sciences Laboratory, a DOE User Facility sponsored by the Office of Biological and Environmental Research. Ni *K*-edge and Fe *K*-edge XAS measurements were carried out at beamline 9-BM of the Advanced Photon Source, a U.S. DOE Office of Science User Facility operated by Argonne National Laboratory under contract DE-AC02-06CH11357. The microscopy work was performed in the Radiological Microscopy Suite (RMS), located in the Radiochemical Processing Laboratory (RPL) at PNNL.

Experimental methods

Sample Growth and Characterization: All epitaxial thin films of $\text{La}_{0.5}\text{Sr}_{0.5}\text{Ni}_{1-x}\text{Fe}_x\text{O}_{3-\delta}$ (LSNFO) solid solutions ($x=0, 0.125, 0.25, 0.375, 0.5$) were grown on (001)-oriented LSAT substrates by OPA-MBE. Experimental setup and growth conditions can be found in ¹⁴. *In situ* XPS was performed on all pristine samples to measure the elemental composition.

Additional XPS at ambient pressure (AP-XPS) was performed at the Advanced Light Source beamline 9.3.2 using an incident photon energy that was calibrated to Au 4f reference. The film surface was cleaned by heating to 300 °C in 100 mTorr O₂, and the surface was deemed clean with the disappearance of C1s feature. Ni 3p and Fe 3p along with La 4d and Sr 3d spectra were collected at 300 °C in 100 mTorr O₂ background at an incident photon energy of 350 eV, corresponding to a shallow inelastic mean free path (IMFP ~0.87 nm). The peaks were fitted with a Shirley background and a Gaussian/Lorentzian (GL30) function except for Ni 3p which was fitted with GL30 modified by an exponential blend (T0.85).

Atomic force microscopy (AFM) was used to examine film surface morphology. The lattice structure was characterized by a high-resolution X-ray diffractometer (Rigaku SmartLab). Cross-sectional STEM samples were prepared using a FEI Helios NanoLab Dual-Beam Focused Ion Beam (FIB) microscope and a standard lift out procedure along the [100] zone axis of the LSAT substrates. STEM high-angle annular dark-field (STEM-HAADF) images were collected on a probe-corrected JEOL GrandARM-300F microscope operating at 300 kV, with a convergence semi-angle of 29.7 mrad. Simultaneous energy-dispersive X-ray spectroscopy (STEM-EDS) mapping was performed to collect composition information from all alloying elements.

Ni *K*-edge and Fe *K*-edge X-ray absorption near-edge structure (XANES) spectra were measured at beamline 9-BM of the Advanced Photon Source at Argonne National Laboratory. X-ray energy was varied by a Si(111) double crystal monochromator and fluorescent x-rays were collected by a four element silicon drift detector. A rhodium coated toroidal mirror was used to focus the x-rays to roughly 0.5 mm in diameter, and a rhodium coated flat mirror was used for harmonic rejection.

After cycling, samples were ultrasonicated in acetone, IPA, and finally DI water for 5 min each to remove dust particles and any remaining salt from the electrolyte. Samples were dried using nitrogen gas, and characterized first by XPS, then AFM.

Electrochemical methods: Electrochemical measurements in a 50 mL Teflon® cell were conducted with a VSP-300 Biologic® potentiostat and Pine® modulated speed rotator (MSR) at room temperature and ambient pressure. A standard three-electrode setup comprised of an assortment of LSNFO working electrodes (where $x = 0, 0.125, 0.25, 0.375, 0.50$), a Pt counter, and an Ag/AgCl reference electrode. The Ag/AgCl reference was calibrated to the RHE in 0.1 M KOH, with all potentials provided in the text reported on the RHE scale. The working electrode was loaded onto a glassy carbon, electrically contacted with a double-sided copper tape, and covered with Kapton tape, exposing a known cross-sectional area of the electrode to the electrolyte.⁴⁴ The electrolyte solution of 0.1 M KOH was prepared in bulk using Semiconductor grade KOH (Sigma-Aldrich) and 18.2 MΩ Millipore water. Electrochemical measurements were performed in O₂ saturated conditions, with scan rates for all CVs being 10 mV/s. The double layer capacitance (C_{DL}) was measured in a non-Faradaic region averaging across the three cycles, extracting the capacitance through the linear relation between current and scan rate.

Reference

1. E. Fabbri, A. Habereder, K. Waltar, R. Kötz and T. J. Schmidt, *Catalysis Science & Technology*, 2014, **4**, 3800-3821.
2. J. Song, C. Wei, Z.-F. Huang, C. Liu, L. Zeng, X. Wang and Z. J. Xu, *Chemical Society Reviews*, 2020, **49**, 2196-2214.
3. J. Suntivich, K. J. May, H. A. Gasteiger, J. B. Goodenough and Y. Shao-Horn, *Science*, 2011, **334**, 1383-1385.
4. X. Cheng, E. Fabbri, Y. Yamashita, I. E. Castelli, B. Kim, M. Uchida, R. Haumont, I. Puente-Orench and T. J. Schmidt, *ACS Catalysis*, 2018, **8**, 9567-9578.
5. J. Hwang, R. R. Rao, L. Giordano, Y. Katayama, Y. Yu and Y. Shao-Horn, *Science*, 2017, **358**, 751-756.
6. D. Liu, P. Zhou, H. Bai, H. Ai, X. Du, M. Chen, D. Liu, W. F. Ip, K. H. Lo, C. T. Kwok, S. Chen, S. Wang, G. Xing, X. Wang and H. Pan, *Small*, 2021, **17**, 2101605.
7. F. Dionigi, T. Reier, Z. Pawolek, M. Gliech and P. Strasser, *ChemSusChem*, 2016, **9**, 962-972.
8. B.-J. Kim, E. Fabbri, M. Borlaf, D. F. Abbott, I. E. Castelli, M. Nachtegaal, T. Graule and T. J. Schmidt, *Materials Advances*, 2021, **2**, 345-355.
9. Q. Guo, X. Li, H. Wei, Y. Liu, L. Li, X. Yang, X. Zhang, H. Liu and Z. Lu, *Frontiers in Chemistry*, 2019, **7**.
10. R. Sankannavar, K. C. Sandeep, S. Kamath, A. K. Suresh and A. Sarkar, *Journal of The Electrochemical Society*, 2018, **165**, J3236-J3245.

11. L. Wang, K. A. Stoerzinger, L. Chang, J. Zhao, Y. Li, C. S. Tang, X. Yin, M. E. Bowden, Z. Yang, H. Guo, L. You, R. Guo, J. Wang, K. Ibrahim, J. Chen, A. Rusydi, J. Wang, S. A. Chambers and Y. Du, *Advanced Functional Materials*, 2018, **28**, 1803712.
12. J. Liu, E. Jia, L. Wang, K. A. Stoerzinger, H. Zhou, C. S. Tang, X. Yin, X. He, E. Bousquet, M. E. Bowden, A. T. S. Wee, S. A. Chambers and Y. Du, *Advanced Science*, 2019, **6**, 1901073.
13. J. Bak, H. Bin Bae and S.-Y. Chung, *Nature Communications*, 2019, **10**, 2713.
14. L. Wang, P. Adiga, J. Zhao, W. S. Samarakoon, K. A. Stoerzinger, S. R. Spurgeon, B. E. Matthews, M. E. Bowden, P. V. Sushko, T. C. Kaspar, G. E. Sterbinsky, S. M. Heald, H. Wang, L. W. Wangoh, J. Wu, E.-J. Guo, H. Qian, J. Wang, T. Varga, S. Thevuthasan, Z. Feng, W. Yang, Y. Du and S. A. Chambers, *Nano Letters*, 2021, **21**, 8324-8331.
15. T. G. Yun, Y. Heo, H. Bin Bae and S.-Y. Chung, *Nature Communications*, 2021, **12**, 824.
16. G. Fu, W. Li, J.-Y. Zhang, M. Li, C. Li, N. Li, Q. He, S. Xi, D. Qi, J. L. MacManus-Driscoll, J. Cheng and K. H. Zhang, *Small*, 2021, **17**, 2006930.
17. J. S. Yoo, X. Rong, Y. Liu and A. M. Kolpak, *ACS Catalysis*, 2018, **8**, 4628-4636.
18. J. Liu, E. Jia, K. A. Stoerzinger, L. Wang, Y. Wang, Z. Yang, D. Shen, M. H. Engelhard, M. E. Bowden, Z. Zhu, S. A. Chambers and Y. Du, *The Journal of Physical Chemistry C*, 2020, **124**, 15386-15390.
19. K. J. May, C. E. Carlton, K. A. Stoerzinger, M. Risch, J. Suntivich, Y.-L. Lee, A. Grimaud and Y. Shao-Horn, *The Journal of Physical Chemistry Letters*, 2012, **3**, 3264-3270.
20. S. Klaus, Y. Cai, M. W. Louie, L. Trotochaud and A. T. Bell, *The Journal of Physical Chemistry C*, 2015, **119**, 7243-7254.
21. I. Spanos, J. Masa, A. Zeradjanin and R. Schlögl, *Catalysis Letters*, 2021, **151**, 1843-1856.
22. S. Anantharaj, S. Kundu and S. Noda, *Nano Energy*, 2021, **80**, 105514.
23. S. Samira, J. Hong, J. C. A. Camayang, K. Sun, A. S. Hoffman, S. R. Bare and E. Nikolla, *JACS Au*, 2021, **1**, 2224-2241.
24. E. Fabbri, M. Nachtegaal, T. Binninger, X. Cheng, B.-J. Kim, J. Durst, F. Bozza, T. Graule, R. Schäublin, L. Wiles, M. Pertoso, N. Danilovic, K. E. Ayers and T. J. Schmidt, *Nature Materials*, 2017, **16**, 925-931.
25. C. Baeumer, J. Li, Q. Lu, A. Y.-L. Liang, L. Jin, H. P. Martins, T. Duchoň, M. Glöß, S. M. Gericke, M. A. Wohlgemuth, M. Giesen, E. E. Penn, R. Dittmann, F. Gunkel, R. Waser, M. Bajdich, S. Nemšák, J. T. Mefford and W. C. Chueh, *Nature Materials*, 2021, **20**, 674-682.
26. A. S. Disa, D. P. Kumah, J. H. Ngai, E. D. Specht, D. A. Arena, F. J. Walker and C. H. Ahn, *APL Materials*, 2013, **1**, 032110.
27. L. Wang, Z. Yang, M. E. Bowden, J. W. Freeland, P. V. Sushko, S. R. Spurgeon, B. Matthews, W. S. Samarakoon, H. Zhou, Z. Feng, M. H. Engelhard, Y. Du and S. A. Chambers, *Advanced Materials*, 2020, **32**, 2005003.
28. L. Wang, L. Chang, X. Yin, L. You, J.-L. Zhao, H. Guo, K. Jin, K. Ibrahim, J. Wang, A. Rusydi and J. Wang, *Applied Physics Letters*, 2017, **110**, 043504.
29. D. Guan, K. Zhang, Z. Hu, X. Wu, J.-L. Chen, C.-W. Pao, Y. Guo, W. Zhou and Z. Shao, *Advanced Materials*, 2021, **33**, 2103392.
30. D. Guan, J. Zhong, H. Xu, Y.-C. Huang, Z. Hu, B. Chen, Y. Zhang, M. Ni, X. Xu, W. Zhou and Z. Shao, *Applied Physics Reviews*, 2022, **9**, 011422.
31. H. Zhang, Y. Gao, H. Xu, D. Guan, Z. Hu, C. Jing, Y. Sha, Y. Gu, Y.-C. Huang, Y.-C. Chang, C.-W. Pao, X. Xu, J.-F. Lee, Y.-Y. Chin, H.-J. Lin, C.-T. Chen, Y. Chen, Y. Guo, M. Ni, W. Zhou and Z. Shao, *Advanced Functional Materials*, 2022, **32**, 2207618.
32. M. W. Louie and A. T. Bell, *Journal of the American Chemical Society*, 2013, **135**, 12329-12337.
33. L. Trotochaud, S. L. Young, J. K. Ranney and S. W. Boettcher, *Journal of the American Chemical Society*, 2014, **136**, 6744-6753.

34. M. B. Stevens, C. D. M. Trang, L. J. Enman, J. Deng and S. W. Boettcher, *Journal of the American Chemical Society*, 2017, **139**, 11361-11364.
35. M. Lyons, L. Russell, M. O'Brien, R. Doyle, I. Godwin and M. Brandon, *International journal of electrochemical science*, 2012, **7**, 2710-2763.
36. D. Friebe, M. W. Louie, M. Bajdich, K. E. Sanwald, Y. Cai, A. M. Wise, M.-J. Cheng, D. Sokaras, T.-C. Weng, R. Alonso-Mori, R. C. Davis, J. R. Bargar, J. K. Nørskov, A. Nilsson and A. T. Bell, *Journal of the American Chemical Society*, 2015, **137**, 1305-1313.
37. C. C. L. McCrory, S. Jung, J. C. Peters and T. F. Jaramillo, *Journal of the American Chemical Society*, 2013, **135**, 16977-16987.
38. D. K. Bediako, B. Lassalle-Kaiser, Y. Surendranath, J. Yano, V. K. Yachandra and D. G. Nocera, *J. Am. Chem. Soc.*, 2012, **134**, 6801-6809.
39. M. L. Weber, G. Lole, A. Kormanyos, A. Schwiers, L. Heymann, F. D. Speck, T. Meyer, R. Dittmann, S. Cherevko, C. Jooss, C. Baeumer and F. Gunkel, *Journal of the American Chemical Society*, 2022, **144**, 17966-17979.
40. O. Q. Carvalho, P. Adiga, L. Wang, J. Liu, E. Jia, Y. Du, S. Nemšák and K. A. Stoerzinger, *Journal of Physics D: Applied Physics*, 2021, **54**, 274003.
41. K. A. Stoerzinger, R. Comes, S. R. Spurgeon, S. Thevuthasan, K. Ihm, E. J. Crumlin and S. A. Chambers, *The Journal of Physical Chemistry Letters*, 2017, **8**, 1038-1043.
42. K. A. Stoerzinger, L. Wang, Y. Ye, M. Bowden, E. J. Crumlin, Y. Du and S. A. Chambers, *Journal of Materials Chemistry A*, 2018, **6**, 22170-22178.
43. J. T. Mefford, X. Rong, A. M. Abakumov, W. G. Hardin, S. Dai, A. M. Kolpak, K. P. Johnston and K. J. Stevenson, *Nature Communications*, 2016, **7**, 11053.
44. P. Adiga and K. A. Stoerzinger, *Journal of Vacuum Science & Technology A*, 2022, **40**, 010801.